Materials Advances

ROYAL SOCIETY OF CHEMISTRY

PAPER

View Article Online
View Journal | View Issue

Check for updates

Cite this: *Mater. Adv.*, 2024, 5, 9774

Promising single crystal host for bulk scintillators: luminescence and energy migration in $(Gd,Y)AlO_3$

Monika Kotyková, *[ab] Romana Kučerková, [a] Alena Beitlerová, [a] Vladimir Babin, [a] Vítězslav Jarý, [a] Jan Touš, [b] Jan Polák, [b] Karel Blažek [b] and Martin Nikl [a]

Received 16th September 2024,
Accepted 12th November 2024

DOI: 10.1039/d4ma00932k

rsc.li/materials-advances

The optical and photoluminescent characteristics of the heavy perovskite $(Gd_{0.40},Y_{0.60})AlO_3$ single crystal were evaluated. Typical Gd^{3+} transitions were observed in the absorption spectrum. The photoluminescent kinetics and temperature dependence of the Gd^{3+} emission line at 312 nm were examined in order to study the energy migration within the Gd^{3+} sublattice. In comparison to multicomponent $(Gd,Y)_3(Ga,Al)_5O_{12}$ garnet, the migration in $(Gd_{0.40},Y_{0.60})AlO_3$ was demonstrated to be more rapid and more efficient at lower temperatures. The radioluminescent spectrum demonstrated the existence of accidental impurities, namely Ce^{3+}, Fe^{3+} and Cr^{3+}, within the primary material, which were subsequently verified through the observation of their distinctive kinetic properties. In excitation spectra within the VUV-UV range at room temperature the band-to-band transition is situated at about 180 nm, in which also an efficient excitation of Ce^{3+} emission occurs. Such a host paves the way to economic industrial production of heavy aluminum perovskite-based single crystal scintillators.

Open Access Article. Published on 12 November 2024. Downloaded on 2/7/2026 10:15:08 PM.
This article is licensed under a Creative Commons Attribution 3.0 Unported Licence.

1. Introduction

The well-known scintillation material $YAlO_3$:Ce (YAP:Ce) is a widely used component in a number of fields, including electron microscopy, X-ray imaging, electron beam inspection systems and medical applications. The most appealing characteristics of this material are its rapid luminescence and scintillation decay time (18–30 ns), minimal afterglow, and favourable proportionality of the response resulting in excellent energy resolution. However, its utilisation is constrained by its low density (5.37 g cm^{-3}), low effective atomic number (Z_{eff} = 32), and a limited light (LY) yield of approximately 20 000 photons per MeV.[1,2] These properties can be enhanced by substituting heavy rare earth ions, such as Lu or Gd, for Y. However, the growth process of $LuAlO_3$:Ce was challenging due to its instability and the frequent appearance of a garnet phase.[3] The perovskite phase was stabilised more effectively by the addition of Y cations to $(Lu,Y)AlO_3$:Ce crystals.[4] Furthermore, industrial-scale crystals of this type were produced later.[5] However, the reported light yield was significantly lower than that of YAP:Ce. This issue was addressed by incorporating Gd^{3+} cations, which stabilised the growth process.[6] The effective atomic number was increased to 64.9 and a competitive light yield of 21 000 photons per MeV was achieved.

It is known that the Gd^{3+} cations act as the energy donor to the majority of rare earth ions, including Ce^{3+}. The energy transfer process $Gd^{3+} \rightarrow Ce^{3+}$ was studied in silicates,[7] garnets,[8] and perovskites.[9]

In $GdAlO_3$:Ce, the bidirectional energy transfer $Gd^{3+} \leftrightarrow Ce^{3+}$ was demonstrated, resulting in a notable reduction in LY.[10] The scintillation kinetics was accelerated from 28 ns in YAP:Ce to 2 ns in $GdAlO_3$:Ce as a consequence of the reverse $Ce^{3+} \rightarrow Gd^{3+}$ energy transfer causing a loss of light yield.[9] Though, up to medium Gd concentration, the reverse energy transfer is not a significant issue in $(Gd,Y)AlO_3$:Ce, and such a material shows an increased density of 6.2 g cm^{-3} and an effective atomic number of approximately 50, which varies depending on the Gd content.[9] Micropullingdown grown small crystals of $Gd_xY_{1-x}AlO_3$:Ce show a comparable light yield for x = 0.5 and x = 0 samples.[11] Fig. 1 shows the comparison of the attenuation coefficient for $(Gd_{0.5},Y_{0.5})AlO_3$ and $YAlO_3$. The values were evaluated using the NIST-XCOM database.[12] The Czech patent[13] proves the possibility of growing $(Gd_y,Y_{1-x-y})AlO_3$:Ce_x crystals with a diameter greater than a few mm using the Czochralski method. This indicates that this material is well suited for high-energy gamma detection, particularly in the form of high-volume detectors with high detection efficiency. The ratio of Gd to Y is in the range y = 0.4–0.6 and the Ce^{3+} content is x = 0.005–0.015. Depending on the Gd/Y ratio, the effective atomic number varies from 45 to 49.

This study focuses on undoped material $(Gd_{0.40},Y_{0.60})AlO_3$, which was grown by the CRYTUR company. The energy migration in the Gd sublattice was investigated by an examination of

[a] *Institute of Physics of the Czech Academy of Sciences, Prague, Czech Republic. E-mail: kotykova@fzu.cz*
[b] *CRYTUR spol. s r. o., Turnov, Czech Republic*

© 2024 The Author(s). Published by the Royal Society of Chemistry

Open Access Article. Published on 12 November 2024. Downloaded on 2/7/2026 10:15:08 PM.
This article is licensed under a Creative Commons Attribution 3.0 Unported Licence.

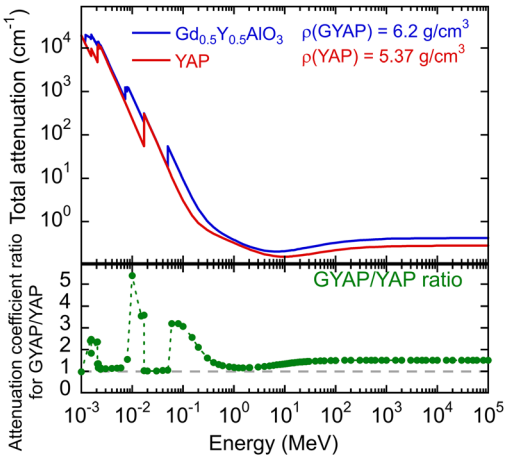

Fig. 1 Total attenuation coefficient according to NIST-XCOM and a ratio of coefficients for $(Gd_{0.5},Y_{0.5})AlO_3$ and $YAlO_3$.

the temperature dependence of the emission intensity and the decay kinetics of the Gd^{3+} 312 nm emission line. The presence of impurities in the initial material is identified and characterised through the analysis of their photoluminescence spectra and decay kinetics.

2. Experimental

The undoped crystal of $(Gd_{0.40}Y_{0.60})AlO_3$ (further noted as (Gd,Y)AlO_3) was prepared using the Czochralski method in the CRYTUR company. The photograph of the sample is in Fig. 2.

The composition was verified by means of microanalysis, using the JEOL JXA-8230 apparatus. For X-ray diffraction (XRD) analysis, the powder diffraction data were collected using the Bragg–Brentano focusing configuration on the powder diffractometer Empyrean of PANalytical (λ_{Cu}, K_α = 1.54184 Å), which was equipped with a fixed divergent slit and a PIXcel3D detector. The sample corresponds to the PDF card 00-060-0774 (PDF 5+ 2024) of the $(Gd_{0.5}Y_{0.5})AlO_3$ compound, see Fig. 3.

A polished plate with dimensions 7 × 7 × 1.4 mm^3 was prepared for optical and luminescence measurements. Absorption spectra were measured with a Shimadzu 3101 PC spectrometer (Shimadzu). A custom-made 5000 M spectrofluorimeter (Horiba Jobin Yvon, Wildwood, MA, USA) equipped with a TBX-04 photon-counting detector (IBH Scotland) and a single-grating monochromator was used for PL and radioluminescence (RL) measurements

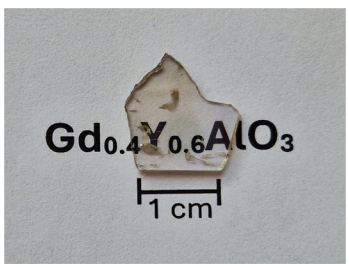

Fig. 2 Photograph of the (Gd,Y)AlO_3 sample.

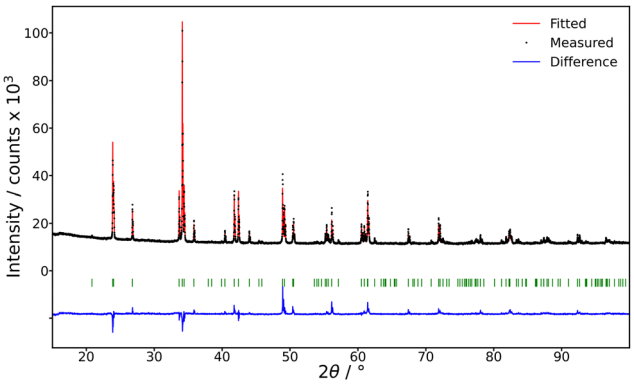

Fig. 3 XRD analysis: the whole pattern profile fit with a fixed structural model (PDF card 00-060-0774) of the measured data. Bragg positions are shown by green vertical bars. The profile fit was reduced to 10–100 2θ.

within the 200–800 nm range. The RL spectra in the far red part of the spectra were measured by the ANDOR (Oxford Instruments) 193 mm focal length Czerny–Turner spectrograph Kymera 193i, equipped with a Back Illuminated CCD detector iDus 420. As excitation sources, the laser driven xenon lamp (EQ-99X LDLSE-nergetic, Hamamatsu Company) for the PL and PLE spectra, and Mo X-ray tube (40 kV, 15 mA, Seifert) for the RL spectra were used. Nanosecond nano-LED pulsed light sources (IBH Scotland) were used to excite fast luminescence decays measured by the time-correlated single-photon counting technique. A microsecond xenon flash-lamp was used for the measurement of slow PL decays using the multichannel scaling method. The measured spectra were corrected for the spectral dependence of excitation energy (PLE) and the spectral dependence of detection sensitivity (RL, PL). To determine the true decay times, the convolution procedure was applied to the decay curves (SpectraSolve software package, Ames Photonics). Measurements within the temperature region of 77–690 K were performed using the high-temperature LN_2 bath cryostat (VPF series, Janis Research Company, Inc., USA); in the region of 9–300 K, a closed-cycle refrigerator (Janis Research Company, Inc., USA) was used.

PLE spectra in the VUV-UV region were measured at the SUPERLUMI station of the P66 beamline at DESY (Hamburg, Germany) under pulsed excitation by synchrotron radiation in the range of 30–330 nm from the PETRA III storage ring. The excitation monochromator is of 2-m normal incidence McPherson-type equipped with a holder for two Al and Pt interchangeable gratings. Excitation spectra were measured with an instrumental resolution of about 0.3 nm. The luminescence was detected by a photomultiplier (Hamamatsu R6358) working in the 185–830 nm range. The samples were located on the cold finger of the He-flow cryostat, enabling temperature regulation in the range of 10–300 K. The excitation spectra are corrected using sodium salicylate.

3. Results and discussion

3.1. Absorption and radioluminescence spectra

An absorption spectrum of the single crystal (Gd,Y)AlO_3 at room temperature is shown in Fig. 4. It can be observed that

Open Access Article. Published on 12 November 2024. Downloaded on 2/7/2026 10:15:08 PM.
This article is licensed under a Creative Commons Attribution 3.0 Unported Licence.

only the lines related to the transitions of Gd^{3+} from the ground state $^8S_{7/2}$ to the higher levels ^6G_J, ^6D_J, ^6I_J, and ^6P_J are observable. The positions of the transitions from the ground state to ^6D_J, ^6I_J, and ^6P_J correspond to the Gd^{3+} absorption lines in Gd-containing undoped aluminum garnets,[14,15] as the position of 4f–4f transition shows only weak dependence on the matrix. The transitions ^8S–^6G_J are clearly observable in the region of 200 nm, whereas in $Gd_2YGaAl_4O_{12}$ garnets, they are obscured by the strong absorption of the host lattice below 220 nm.[15]

In the measured radioluminescence spectrum, all dominant emission lines below 320 nm can be ascribed to the transitions of Gd^{3+} from higher levels to the ground state; see Fig. 5. The transitions $^6G_{7/2}$–^6P_J are placed in the region 550–650 nm and $^6G_{5/2}$–$^6I_{7/2}$ above 700 nm. In addition to the Gd^{3+} lines, some impurity emissions can be seen. The broad band with a maximum at approximately 350 nm is attributed to the 5d–4f transition of Ce^{3+}, typical for aluminum perovskite hosts.[6,9,16] Moreover, the accidental impurities Cr^{3+} and Fe^{3+} are responsible for the emission observed above 700 nm that will be discussed in greater detail later.

3.2. Photoluminescence spectra

The emission and excitation spectra illustrated in Fig. 6 were obtained at room temperature for a range of excitation and emission wavelengths. As expected, the well-known Gd^{3+} emission at 312 nm was observed under 271 nm excitation (see black line in Fig. 6(a)). The corresponding PL excitation spectrum of Gd^{3+}, as illustrated in Fig. 6(b), is in agreement with the absorption spectrum, which demonstrates all transitions to higher 4f levels of Gd^{3+}. The excitation spectrum for 589 nm emission confirms the occurrence of transitions originating from the ^6G_J levels around 200 nm. The emission spectra presented in Fig. 6(a), excited at 271, 310 and 370 nm, indicate the potential presence of impurities or defects in the material. The presence of Ce^{3+}, Cr^{3+}, and Fe^{3+} will be demonstrated also by their typical kinetic behaviour later.

In addition to the Gd^{3+} emissions illustrated in Fig. 6(a), the emission from Ce^{3+} at 360 nm can be observed. The position is consistent with that observed in the radioluminescence spectrum.

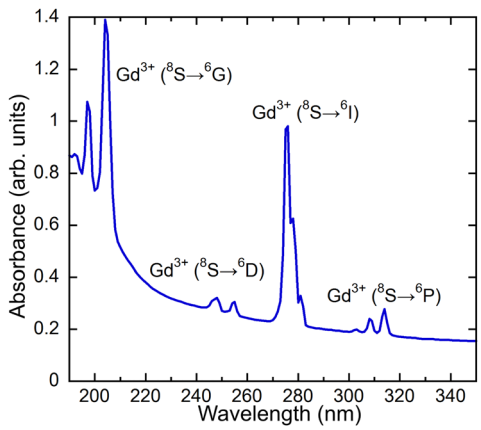

Fig. 4 Absorption spectrum of $(Gd,Y)AlO_3$.

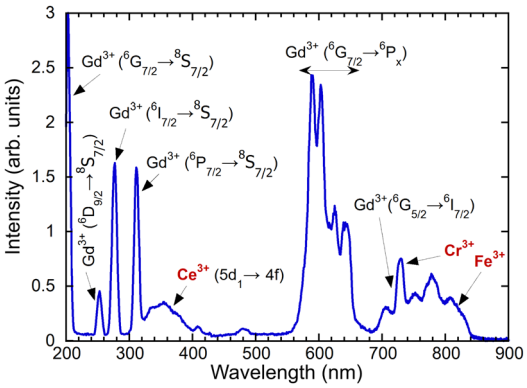

Fig. 5 Radioluminescence spectrum of $(Gd,Y)AlO_3$, X-ray excitation, 40 kV, 15 mA.

Fig. 6(c) shows the excitation spectrum for the emission of Ce^{3+} at 354 nm. The peaks observed at 191, 200 and 271 nm demonstrate the energy transfer from Gd^{3+} towards Ce^{3+}. Direct excitations of Ce^{3+} ions are also noticeable matching the Ce^{3+} 4f–5d absorption bands in heavy aluminum perovskites.[17]

The sharp emission line at 725 nm can be attributed to Cr^{3+} in perovskites, as evidenced by previous studies.[18,19] As illustrated in Fig. 6(b), the excitation spectrum demonstrates the energy transfer from Gd^{3+} to Cr^{3+}, as previously reported in $GdAlO_3$[20] and garnets.[21] The low concentration of Cr^{3+} ions in the initial material precludes the observation of typical excitation bands.

Another common impurity in oxide crystals such as YAP, YAG and Al_2O_3 is Fe^{3+}.[22,23] Typically, the emission occurs at approximately 750 nm. As illustrated in Fig. 6(c), the presence of only Gd^{3+} lines is indicative of the infrequent occurrence of Fe^{3+}.

The radioluminescence spectrum exhibited emissions from Ce^{3+}, Cr^{3+}, and Fe^{3+}, which were also observed in the PL spectra. In contrast, the broad emission band with a maximum at 525 nm in the emission spectrum depicted in Fig. 6 is not observable in radioluminescence. The position of the band corresponds to that of Mn^{2+} ions in YAP:Ce.[24,25] The measured decay time does not correspond to typical Mn values as will be discussed below. Typically, excitation spectra of Mn^{2+} exhibit a sharp excitation band at approximately 410 nm, accompanied by slow decay kinetics around 3.5 ms.[26] As can be observed in Fig. 6(c), the excitation spectrum of 525 nm emission exhibits two broad bands at 310 and 380 nm. We note that in gamma irradiated YAP an induced broad absorption band at 400 nm was identified (close to the excitation band at 380 nm in Fig. 6(c)) and ascribed to an F^+ center located close to the cation vacancy.[22]

3.3. Photoluminescence decay

The energy migration in the Gd sublattice can be characterized by the decay of the Gd^{3+} 312 nm emission line. Fig. 7 illustrates the decay curve of $(Gd,Y)AlO_3$ at room temperature. The decay curve was approximated with an exponential function composed of the rise time and decay time components:

$$I(t) = -A_1 \exp(-t/\tau_r) + A_2 \exp(-t/\tau) \quad (1)$$

© 2024 The Author(s). Published by the Royal Society of Chemistry

Open Access Article. Published on 12 November 2024. Downloaded on 2/7/2026 10:15:08 PM.
This article is licensed under a Creative Commons Attribution 3.0 Unported Licence.

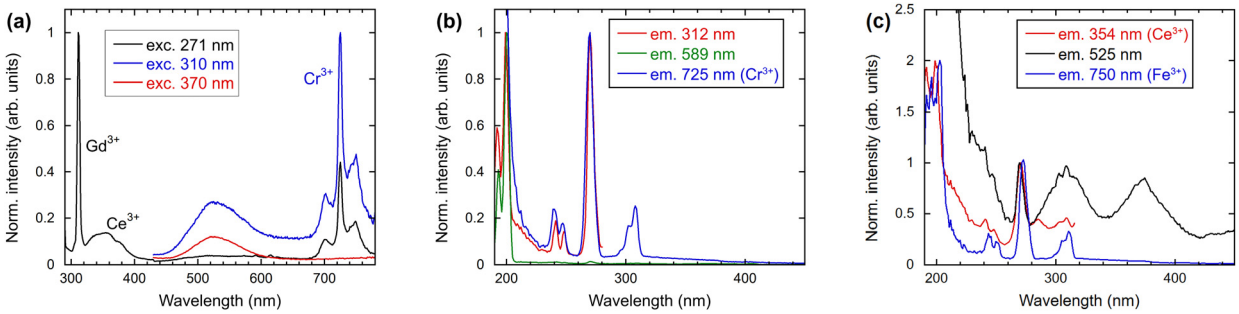

Fig. 6 (a) Emission spectra, excitation wavelengths 271, 310 and 370 nm; (b) excitation spectra, emission wavelengths 312, 589 and 725 nm; (c) excitation spectra, emission wavelengths 354, 525 and 750 nm.

where I is the luminescence intensity, t is time, τ_r is the rise time, τ is the decay time and A_1, A_2 are constants. The rise time of 3.72 μs can be attributed to the ^6I_J–^6P_J level transition of Gd^{3+}. The measured decay time from the ^6P_J level to the ground state is 67.4 μs. In $GdY_2GaAl_4O_{12}$ garnets with comparable Gd content, the measured decay time of the 312 nm line can be estimated to be approximately 3.2 ms. In fully Gd-concentrated $Gd_3GaAl_4O_{12}$ garnet, the decay time was observed to be 31 μs.[27] This suggests that the rate of energy transfer within the Gd sublattice of aluminum perovskite is more than one order of magnitude faster than in aluminum garnets. One potential explanation is related to the number and distances among Y cations in the host structure. By using the structural parameters from ICSD #99419, in $YAlO_3$ there are six neighboring Y cations located at a distance of 3.63–3.80 Å, whereas in $Y_3Al_5O_{12}$, only four other Y cations are at a distance of 3.68 Å (ICSD#67103). The critical distance in the Gd^{3+}–Gd^{3+} energy transfer scale with distance ($\propto 1/r^{10}$) due to the strongly forbidden transitions of the Gd^{3+} ions, which may account for the observed difference.

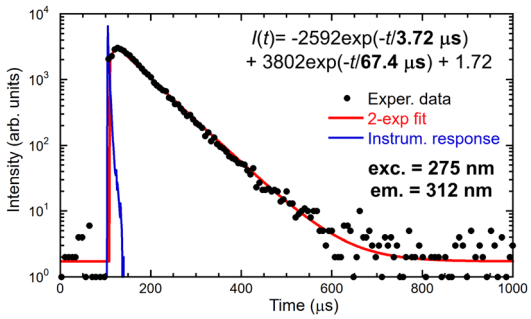

Fig. 7 Decay curve of 312 nm emission of Gd^{3+}, the measured data are the convolution of IRF and decay equation in the figure.

Table 1 Decay curve parameters for varying excitation and emission wavelengths. The decay curve is a convolution of instrumental response and a fit in a form $I(t) = -A_1 \exp(-t/\tau_r) + \sum_i A_i \exp(-t/\tau_i) +$ background. The error of decay time τ_i values is of the order of 1% or less

	Exc. (nm)	Em. (nm)	τ_r (μs)	τ_1 (μs)	τ_2 (μs)
Ce^{3+} (5d → 4f)	266	350		0.002 (60%)	0.014 (40%)
Gd^{3+} (^6D_J → $^8S_{7/2}$)	241	278	6.5	17.0 (100%)	
Gd^{3+} (^6I_J → $^8S_{7/2}$)	275	312	3.7	67.4 (100%)	
Gd^{3+} → Ce^{3+}	271	350		15.1 (54%)	62.5 (46%)
Gd^{3+} → defect	271	522		32.2 (74%)	109.6 (26%)
Gd^{3+} ($^6G_{7/2}$ → ^6P_J)	203	590		35.0 (97%)	1470 (3%)
Gd^{3+} → Cr^{3+}	310	723		81.9 (23%)	18 200 (77%)

Directly excited emission of Ce^{3+} shows acceleration in the first component of 2 ns as a result of energy transfer towards Gd^{3+}, see Table 1. The second component of 14 ns is consistent with the known decay time of Ce^{3+} in YAP:Ce. The energy transfer from Gd^{3+} to Ce^{3+} is demonstrated by the existence of a slow component in Ce^{3+} decay when excited through the Gd^{3+} sublattice at 271 nm.

The decay time of Cr^{3+} in YAP was reported of 34 ms coming from a couple of R-lines at about 725 nm.[18] The dominant decay time for this emission at 723 nm was then measured of 18.2 ms in $(Gd,Y)AlO_3$, see Table 1. Such a difference might arise from different electron–phonon interaction in the $(Gd,Y)AlO_3$ host compared to YAP which is determining the transition dipole moment.[28]

The measured decay curve at 522 nm can be described by two components, with decay time values of 32.2 and 109.6 μs. The absence of a long decay component in the ms time scale, typical for Mn^{2+} ions,[26] points to a different emission center attributed by us to an unidentified defect within the crystal structure.

3.4. VUV-UV excitation

This section presents a comparative analysis of the excitation spectra of $(Gd,Y)AlO_3$ and other materials under VUV-UV excitation at the synchrotron in DESY, Hamburk. Fig. 8 illustrates the excitation spectra for Gd^{3+} and Ce^{3+} emission in the VUV-UV range at room temperature and 10 K. The energy transfer to Ce^{3+} is evidenced from the excitation spectrum for 370 nm emission. In all excitation spectra, sharp Gd^{3+} lines in the range of 185–210 nm can be observed, as well as around 250 and 280 nm. The peak of the broad VUV excitation band may be indicative of a band-to-band transition in the host. From its position, an estimate of the energy gap (E_g) can be made. At 10 K, the band-to-band transition is observed at 160 nm

Open Access Article. Published on 12 November 2024. Downloaded on 2/7/2026 10:15:08 PM.
This article is licensed under a Creative Commons Attribution 3.0 Unported Licence.

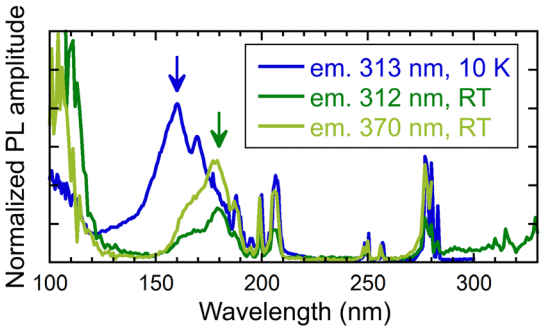

Fig. 8 Excitation spectra measured for different emission wavelengths (313 and 370 nm) and temperature 10 K and RT. Measured at the PETRA III storage ring.

(illustrated by the blue arrow in Fig. 8), which is in accordance with the findings of previous research.

At the same temperature, the transition was observed at 7.85 eV (158 nm) in YAP, at 7.07 eV (175 nm) in $GdAlO_3$ and at 7.59 eV (163 nm) in $Y_{0.85}Gd_{0.15}AlO_3$.[29] In contrast to YAP, the emission of excitons is not detectable in $(Gd,Y)AlO_3$ due to the energy transfer from excitons to Gd^{3+}, as observed in garnets.[30] In perovskite $YAlO_3$, exciton emission was observed at 220 and 301 nm.[31] These emissions were ascribed to excitons that are localised in proximity to Y_{Al}^{3+}-related defects.[31] At room temperature, the band-to-band transition is shifted to 178 nm (green arrow in Fig. 8).

3.5. Temperature dependence

The intensity of the photoluminescence emission depends on the efficiency of energy migration within the Gd^{3+} sublattice, which is a function of temperature. Fig. 9 shows the dependence of the integrals of the PL spectra in the range of 295–325 nm and the decay time on the temperature. The values were normalised in order to enable comparison of their decrease in the low-temperature region. Fig. 10 illustrates the decay curves of the Gd^{3+} ions in $(Gd,Y)AlO_3$ at varying temperatures. As the temperature increases from the lowest values, the decay time decreases. The rise time component was found to be approximately 50 μs in the range of 9–40 K. In the range of 60–690 K, a slight decrease in the rise time was observed.

It has been observed that the integral of emission and the decay time exhibit similar behaviour up to a temperature of 300 K. The observed decrease in emission intensity can be

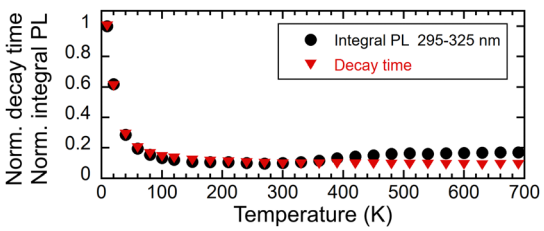

Fig. 9 Temperature dependence of a normalised integral of PL spectra in the range of 295–325 nm excited with 275 nm and normalised PL decay time (exc. 275 nm, em. 312 nm), both norm. at 9 K.

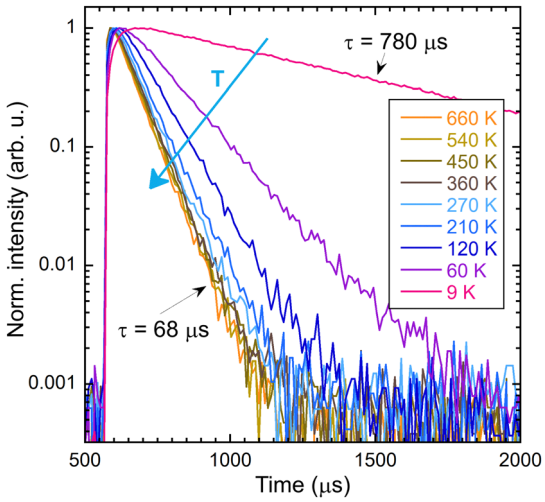

Fig. 10 Decay curves of the intrinsic Gd^{3+} emission 312 nm as a function of temperature; the sample was excited at 275 nm.

explained in terms of energy migration within the Gd^{3+} sublattice. The energy transfer process is dependent on the assistance of lattice phonons, and thus becomes less efficient at low temperatures. As the temperature increases, the migration process becomes more efficient, involving the participation of numerous lattice constants. Subsequently, the non-radiative transfer of energy to defects, which results in energy loss, becomes more probable, leading to an acceleration in the decay process.

In contrast to the Ce-doped multicomponent garnets, migration remains effective at 9 K in $(Gd,Y)AlO_3$ with a decay time of 780 μs that is faster than the expected decay time of Gd^{3+} in the order of ms. The migration of energy in garnets is limited up to 100 K. In $Gd_3Ga_3Al_2O_{12}$, the migration process becomes frozen around 60 K.[15] In $Gd_2YGaAl_4O_{12}$, the PL intensity at a temperature of 8 K is approximately 25× higher than the intensity at 300 K. The temperature at which migration is frozen in $(Gd,Y)AlO_3$ is unknown. However, the PL intensity at 9 K is approximately ten times higher than at 300 K. It can be reasonably assumed that the ratio would be even higher if migration were still effective at the lowest temperature.

The observed increase in PL emission above 280 K is most probably caused by a combination of three factors. The first factor may be attributed to the presence of a shallow trap operating near room temperature. Thermal detrapping from such a trap at higher temperatures would return the charge carrier back to the energy migration process and increase the observed emission intensity. The second factor is an experimental artifact caused by the movement of the sample holder with a change in temperature causing an optical misalignment. The third potential contributor is a temperature-dependent absorption spectrum, as illustrated in Fig. 11. In examining the temperature dependence of the integral of absorption spectra within the range of 265–285 nm, a slight increase was observed. However, this change did not correlate with the intensity of emission (see inset in Fig. 11). Therefore, this contribution to the PL emission intensity increase can be considered minor.

© 2024 The Author(s). Published by the Royal Society of Chemistry

Open Access Article. Published on 12 November 2024. Downloaded on 2/7/2026 10:15:08 PM.
This article is licensed under a Creative Commons Attribution 3.0 Unported Licence.

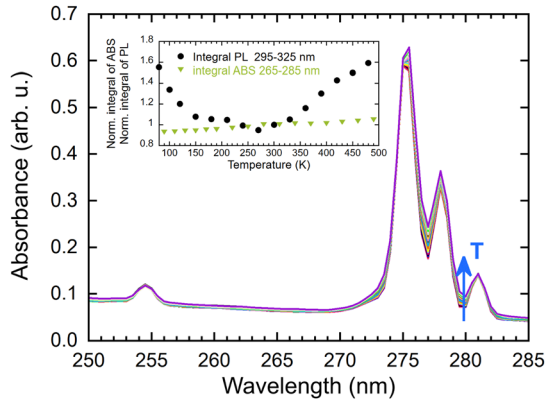

Fig. 11 Absorption spectra as a function of temperature (77–490 K), inset: normalised integral of absorbance and PL spectra in a range of 265–285 nm (norm. at 300 K).

4. Conclusions

An undoped crystal of heavy aluminum perovskite $(Gd_{0.40},Y_{0.60})AlO_3$ was prepared by the Czochralski method and its optical and luminescence characteristics were studied. Typical Gd^{3+} transitions were observed in the absorption, radioluminescence, and photoluminescence spectra. The energy migration in the Gd-sublattice was monitored by analysing the Gd^{3+} PL decay kinetics. The presence of the Cr^{3+}, Fe^{3+} and Ce^{3+} impurities was verified by means of RL, PL and PLE spectra, as well as through the observation of their typical characteristic decay kinetics. The transfer of energy from Gd^{3+} to Ce^{3+} was demonstrated through the examination of the PLE and decay kinetics features. The temperature dependence of the photoluminescence spectra and the decays of the Gd^{3+} 312 nm emission line were examined to study energy migration in the Gd sublattice. This dependence demonstrated that it is more efficient in the perovskite structure compared to that of the garnet structure. The observed decrease in PL intensity is accompanied by an acceleration of the PL decay of the 312 nm emission line. The comparable energy migration speed in the Gd sublattice in $Gd_{0.4}Y_{0.6}AlO_3$ and fully concentrated GAGG garnet, along with the effective energy transfer from the host towards an accidental Ce^{3+} impurity of extremely low concentration, indicates the potential for the $(Gd,Y)AlO_3$ host crystal to be used as an effective scintillator with optimized Ce^{3+} doping. This will be the subject of future research.

Data availability

Data are available upon request from the corresponding author, and they will also be appended to the gold open access reprint with an independent doi.

Conflicts of interest

There are no conflicts to declare.

Acknowledgements

This research was supported by the project no. FW06010047 of Technological Agency of the Czech Republic. We would like to acknowledge DESY (Hamburg, Germany), a member of the Helmholtz Association HGF, for the provision of experimental facilities. Parts of this research were carried out at PETRA III and we would like to thank Dr Aleksei Kotlov for assistance in using P66 (PETRA III facility). Beamtime was allocated for proposal I-20221111 EC. We would like to express our gratitude to Markéta Jarošová and Karel Jurek for conducting the sample composition microanalysis and to Jan Rohlíček for undertaking the XRD measurement.

Notes and references

1 M. Moszynski, M. Kapusta, D. Wolski, W. Klamra and B. Cederwall, *Nucl. Instrum. Methods Phys. Res., Sect. A*, 1998, **404**, 157–165.
2 F. Moretti, K. Hovhannesyan, M. Derdzyan, G. A. Bizarri, E. D. Bourret, A. G. Petrosyan and C. Dujardin, *ChemPhysChem*, 2017, **18**, 493–499.
3 W. Moses, S. Derenzo, A. Fyodorov, M. Korzhik, A. Gektin, B. Minkov and V. Aslanov, *IEEE Trans. Nucl. Sci.*, 1995, **42**, 275–279.
4 A. Petrosyan, G. Shirinyan, K. Ovanesyan, C. Pedrini and C. Dujardin, *J. Cryst. Growth*, 1999, **198–199**, 492–496.
5 J. Trummer, E. Auffray, P. Lecoq, A. Petrosyan and P. Sempere-Roldan, *Nucl. Instrum. Methods*, 2005, **551**, 339–351.
6 M. Pokorný, V. Babin, A. Beitlerová, K. Jurek, J. Polák, J. Houžvička, D. Panek, T. Parkman, V. Vaněček and M. Nikl, *NPG Asia Mater.*, 2021, **13**, 66.
7 E. Bosze, G. Hirata, L. Shea-Rohwer and J. McKittrick, *J. Lumin.*, 2003, **104**, 47–54.
8 M. Kučera, M. Nikl, M. Hanuš and Z. Onderisinova, *Phys. Status Solidi RRL*, 2013, **7**, 571–574.
9 M. Kučera, M. Rathaiah, A. Beitlerová, R. Kučerková and M. Nikl, *IEEE Trans. Nucl. Sci.*, 2020, **67**, 1049–1054.
10 J. A. Mareš, M. Nikl, C. Pedrini, D. Bouttet, C. Dujardin, B. Moine, J. W. M. Verweij and J. Kvapil, *Radiat. Eff. Defects Solids*, 1995, **135**, 369–373.
11 K. Kamada, T. Endo, K. Tsutsumi and A. Yoshikawa, *Phys. Status Solidi C*, 2012, **9**, 2263–2266.
12 S. Seltzer, XCOM-Photon Cross Sections Database, NIST Standard Reference Database 8, 1987, **https://www.nist.gov/pml/data/xcom/index.cfm**.
13 K. Blažek, M. Nikl, J. Touš, K. Bartoš, J. Polák and T. Marek, A method of producing a crystal for a scintillation crystal detector and a crystal for a scintillation crystal detector, Czech patent no. 309877, 2022.
14 D. Spassky, F. Fedyunin, E. Rubtsova, N. Tarabrina, V. Morozov, P. Dzhevakov, K. Chernenko, N. Kozlova, E. Zabelina, V. Kasimova and O. Buzanov, *Opt. Mater.*, 2022, **125**, 112079.
15 K. Bartosiewicz, V. Babin, K. Kamada, A. Yoshikawa and M. Nikl, *J. Lumin.*, 2015, **166**, 117–122.

© 2024 The Author(s). Published by the Royal Society of Chemistry

Open Access Article. Published on 12 November 2024. Downloaded on 2/7/2026 10:15:08 PM.
This article is licensed under a Creative Commons Attribution 3.0 Unported Licence.

16 M. J. Weber, *J. Appl. Phys.*, 1973, **44**, 3205–3208.
17 E. Mihóková, M. Nikl, M. Bacci, M. Dušek and V. Petříček, *Phys. Rev. B*, 2009, **79**, 195130.
18 M. J. Weber, *J. Appl. Phys.*, 1973, **44**, 4058–4064.
19 M. Yamaga, H. Takeuchi, T. P. J. Han and B. Henderson, *J. Phys.: Condens. Matter*, 1993, **5**, 8097–8104.
20 A. De Vries, W. Smeets and G. Blasse, *Mater. Chem. Phys.*, 1987, **18**, 81–92.
21 S. Vargas and D. Hamilton, *J. Lumin.*, 1997, **72–74**, 904–905.
22 Y. Dong, J. Xu, G. Zhou, G. Zhao, L. Su, X. Xu, H. Li and J. Si, *Phys. Status Solidi A*, 2007, **204**, 608–612.
23 S. R. Rotman, C. Warde, H. L. Tuller and J. Haggerty, *J. Appl. Phys.*, 1989, **66**, 3207–3210.
24 M. A. Noginov, G. B. Loutts and M. Warren, *J. Opt. Soc. Am. B*, 1999, **16**, 475.
25 Y. Zhydachevskii, I. Kamińska, K. Fronc, A. Reszka, W. Paszkowicz, S. Warchol, M. Berkowski, D. Elbaum and A. Suchocki, *Opt. Mater.*, 2014, **37**, 125–131.
26 Y. Zhydachevskii, A. Luchechko, D. Maraba, N. Martynyuk, M. Glowacki, E. Bulur, S. Ubizskii, M. Berkowski and A. Suchocki, *Radiat. Meas.*, 2016, **94**, 18–22.
27 V. Babin, M. Nikl, K. Kamada, A. Beitlerová and A. Yoshikawa, *J. Phys. D: Appl. Phys.*, 2013, **46**, 365303.
28 Z. Wen-Chen, L. Bang-Xing, F. Guo-Ying and L. Hong-Gang, *J. Lumin.*, 2013, **138**, 214–217.
29 Y. Zhydachevskii, Y. Hizhnyi, S. G. Nedilko, I. Kudryavtseva, V. Pankratov, V. Stasiv, L. Vasylechko, D. Sugak, A. Lushchik, M. Berkowski, A. Suchocki and N. Klyui, *J. Phys. Chem. C*, 2021, **125**, 26698–26710.
30 V. Khanin, I. Venevtsev, K. Chernenko, V. Pankratov, K. Klementiev, T. Van Swieten, A. J. Van Bunningen, I. Vrubel, R. Shendrik, C. Ronda, P. Rodnyi and A. Meijerink, *J. Lumin.*, 2021, **237**, 118150.
31 V. Babin, V. Gorbenko, I. Kondakova, T. Kärner, V. V. Laguta, M. Nikl, S. Zazubovich and Y. Zorenko, *J. Phys. D: Appl. Phys.*, 2011, **44**, 315402.

© 2024 The Author(s). Published by the Royal Society of Chemistry